

# Complex Multipatch Rupture and Aftershock Characteristics of the 2024 $M_w$ 4.2 Buan, Korea, Earthquake Sequence

OPEN  ACCESS

Min-Seong Seo<sup>1</sup> , Won-Young Kim<sup>2</sup> , Sangwoo Han<sup>1</sup> , Jun Yong Park<sup>1</sup> , and YoungHee Kim<sup>\*1</sup> 

## Abstract

Moderate-magnitude earthquakes in stable continental regions (SCRs) can pose significant hazards, yet their rupture processes remain poorly understood due to sparse instrumentation and their infrequent occurrence. The 2024  $M_w$  4.2 Buan, Korea, earthquake, and its aftershock sequence were exceptionally well recorded by a local seismic network, providing a rare opportunity to investigate the rupture process of a moderate-magnitude earthquake in an SCR. Focal mechanisms and high-precision relocations reveal multiple fault strands activated during the eight-month-long sequence. Using an aftershock as an empirical Green's function, we retrieve relative source time functions of the mainshock, which are subsequently used to construct a detailed slip model. We apply two different rupture modeling approaches: a two-patch modeling with elliptical subfaults and a linear slip inversion. Both approaches consistently reveal two spatially distinct, high-stress-drop patches that ruptured sequentially, with a short temporal overlap, indicating notable rupture complexity. Furthermore, both on-fault and off-fault aftershocks appear to have been triggered by static stress increases associated with the mainshock rupture.

**Cite this article as** Seo, M.-S., W.-Y. Kim, S. Han, J. Y. Park, and Y. Kim (2025). Complex Multipatch Rupture and Aftershock Characteristics of the 2024  $M_w$  4.2 Buan, Korea, Earthquake Sequence, *Seismol. Res. Lett.* **XX**, 1–15, doi: [10.1785/0220250261](https://doi.org/10.1785/0220250261).

## Supplemental Material

## Introduction

On 11 June 2024, an  $M_w$  4.2 earthquake struck near Buan, in the southwestern part of the Korean Peninsula (KP; Fig. 1a). The mainshock was widely felt across South Korea, with a peak ground acceleration of 0.13g recorded at the nearest station, PUAA ( $\Delta = 3.4$  km, Az. = 350°). This earthquake was the largest in southwestern Korea since the 1980s, when reliable earthquake catalogs first became available for the region. A foreshock of  $M_L$  0.5 preceded the mainshock by about 28 min, followed by 36 aftershocks through 13 February 2025, according to the Korea Meteorological Administration (KMA). Southern KP lies within a stable continental region (SCR) and is characterized by negligible tectonic strain rates and low seismicity (Fig. 1a; Jin *et al.*, 2006; Lee *et al.*, 2022). This earthquake was well recorded by stations with good coverage, providing an opportunity to address several questions about the rupture processes of such a moderate-sized earthquake in an SCR setting.

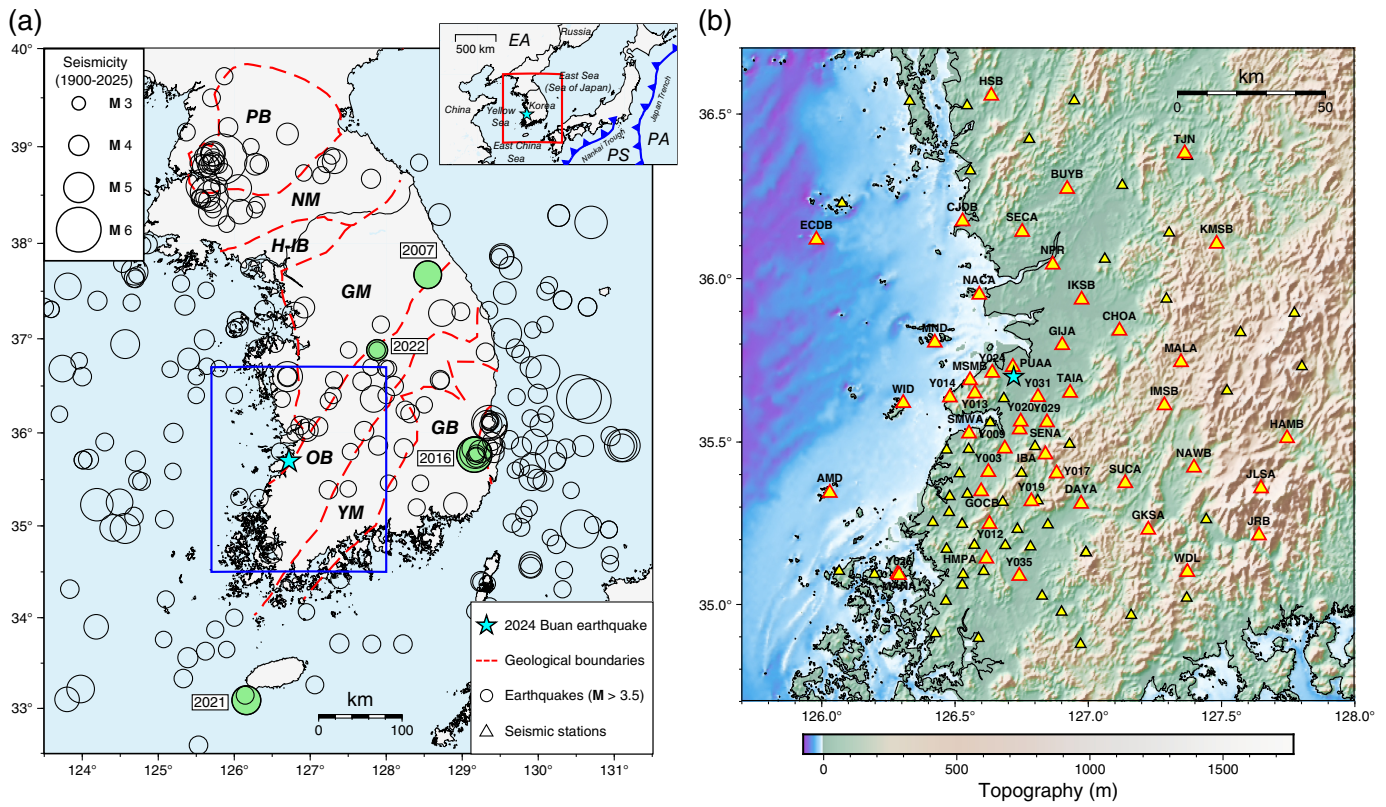
The rupture process of moderate-size earthquakes in SCRs remains poorly understood, primarily due to limited seismic station coverage and the infrequent occurrence of such events. However, in recent years, improved seismic networks with adequate station coverage have enabled detailed studies that reveal features such as complex slip distributions (e.g., Pennington, Chang, *et al.*, 2022; Neves *et al.*, 2024), multiple

subevents (Horton *et al.*, 2015; Meng *et al.*, 2021), and unusually high stress drops compared to global averages (e.g., Viegas *et al.*, 2010; Boyd *et al.*, 2017). Specific case studies from SCRs globally clearly demonstrate these recurring features, including rupture complexity and high stress drops. For example, in Eastern North America, the 2011  $M_w$  5.8 Mineral, Virginia, earthquake exhibited a complex rupture comprising three subevents (Chapman, 2013; Hartzell *et al.*, 2013) and stress drops of 25–67 MPa (Hartzell *et al.*, 2013; Wu and Chapman, 2017). In Europe, the 2019  $M_w$  4.9 Le Teil earthquake in southeastern France showed a heterogeneous slip distribution, rupturing at least three asperities (Godano *et al.*, 2025). In southern KP, the 2016  $M_w$  5.4 Gyeongju earthquake ruptured on multiple slip patches, with an average stress drop of 23 MPa (Uchide and Song, 2018). Dynamic rupture simulations further indicate that both high stress drop and elevated fracture energy were needed

1. School of Earth and Environmental Sciences, Seoul National University, Seoul, Republic of Korea,  <https://orcid.org/0000-0001-7043-8938> (M-SS);  <https://orcid.org/0000-0001-5832-7127> (SH);  <https://orcid.org/0000-0003-2244-0210> (JYP);  <https://orcid.org/0000-0002-1111-632X> (YHK); 2. Lamont-Doherty Earth Observatory of Columbia University, Palisades, New York, U.S.A.,  <https://orcid.org/0000-0002-0005-9681> (W-YK)

\*Corresponding author: youngkim@snu.ac.kr

Copyright © 2025. The Authors. This is an open access article distributed under the terms of the CC-BY license, which permits unrestricted use, distribution, and reproduction in any medium, provided the original work is properly cited.



to reproduce observed near-source ground motions (Song and Duan, 2024). More recently, the 2022  $M_w$  3.8 Goesan earthquake and its foreshock ( $M_w$  3.5) exhibited unusually high stress drops of 107 and 84 MPa, respectively, based on corner-frequency analysis and aftershock spatial distributions (Kim et al., 2023). Even with limited station coverage, the 2007  $M_w$  4.6 Odaesan earthquake showed signs of rupture complexity (Kim et al., 2010). Similarly, the 2021  $M_w$  4.9 offshore Jeju Island earthquake involved at least two nucleation phases followed by two major subevents, as inferred from both local and regional waveforms (Han, Kim, Lim, et al., 2024).

Although these recent studies suggest that rupture complexity and high stress drop are recurring features of moderate-size earthquakes in SCR, such characteristics are not universal. For instance, the 2024  $M_w$  4.8 Tewksbury, New Jersey, earthquake exhibited a relatively simple rupture and a range of stress drop from 6.6 MPa (Han, Kim, Park, et al., 2024) to a moderate 20 MPa (Beaucé et al., 2025). Similarly, the 2022  $M_w$  3.8 Goesan earthquake showed no clear evidence of rupture complexity or directivity (Kim et al., 2023). Such variability may reflect differences in source properties, but could also result from limitations in data quality and station coverage. Most previous studies have relied on regional or teleseismic data because local station density has typically been low near the epicenters of unexpected events. This has limited the resolution of rupture models, particularly in the fault dip direction, where local body waves provide superior sensitivity. Some studies have utilized single-station waveform analyses to constrain rupture directivity

**Figure 1.** (a) Seismicity and geological boundaries of the Korean Peninsula (KP). Epicenters of shallow earthquakes (magnitudes  $\geq 3.5$ ) that occurred between 1900 and 2025 are shown. The cyan star marks the hypocenter of the 2024 Buan mainshock. Green-filled circles denote the epicenters of notable events, including the 2007 Odaesan, 2016 Gyeongju, 2021 Jeju Island, and 2022 Goesan earthquakes. Geological unit boundaries are shown as red-dashed lines (Kee et al., 2019). Major geologic units of the KP are abbreviated as follows: GB, Gyeongsang basin; GM, Gyeonggi massif; H-Ib, Hongseong-Imjingang belt; NM, Nangrim massif; OB, Ogneon fold belt; PB, Pyeongnam basin; and YM, Yeongnam massif. The inset map shows the tectonic setting of East Asia, with the study area outlined in red. Plate abbreviations: EA, Eurasian plate; PA, Pacific plate; PS, Philippine Sea plate. (b) Distribution of seismic stations used in this study, overlaid on regional topography and bathymetry. Yellow triangles indicate the locations of seismic stations; those used in the slip inversion are outlined in red. The color version of this figure is available only in the electronic edition.

(Yao et al., 2025). However, these approaches remain limited in their ability to resolve the fine kinematic details of rupture processes. Consequently, despite these advances, systematic analyses of moderate-size SCR earthquakes recorded by dense local networks are still rare, leaving the diversity of rupture behaviors largely unexplored. Therefore, to better assess rupture diversity in SCR settings, it is essential to examine more events with dense local seismic recordings.

In contrast to many past moderate-sized earthquakes in KP, the 2024 Buan earthquake sequence was well recorded by

TABLE 1  
**Focal Mechanisms of Major ( $M \geq 2$ ) Events**

| ID  | $M_w$ | Nodal Plane 1 |         |          | Nodal Plane 2 |         |          | $P$ Axis    | $T$ Axis    |
|-----|-------|---------------|---------|----------|---------------|---------|----------|-------------|-------------|
|     |       | Strike (°)    | Dip (°) | Rake (°) | Strike (°)    | Dip (°) | Rake (°) | $tr/pl$ (°) | $tr/pl$ (°) |
| 2*  | 4.23  | 220           | 73      | -160     | 124           | 71      | -18      | 82/26       | 352/1       |
| 17* | 2.93  | 201           | 32      | 144      | 322           | 72      | 63       | 72/22       | 198/55      |
| 29† | 2.37  | 212           | 73      | -166     | 118           | 77      | -17      | 74/22       | 165/2       |
| 38† | 2.38  | 225           | 70      | -173     | 133           | 83      | -20      | 87/19       | 180/9       |

\*Seismic moments and focal mechanisms are derived from waveform modeling.

†Seismic moments are obtained from spectral fitting, and focal mechanisms are from  $P$ -wave first motions.

nearby permanent stations with sufficient azimuthal coverage, enabling a high-resolution rupture model for a complex mainshock. In this study, we first determine the focal mechanisms of significant earthquakes and delineate the geometry of the fault system by high-precision hypocenter relocations. We then retrieve relative source time functions (RSTFs) at stations with broad azimuthal coverage to infer the mainshock rupture process. We successfully model the complex mainshock rupture as two elliptical patches using the RSTFs, which eliminates path and site effects from the observed records. Finally, we discuss the underlying physical mechanisms of the observed rupture complexity and its role in aftershock triggering in a complex fault system with multiple segments.

## 11 June 2024 Buan, Korea, Earthquake Sequence

To characterize the fault geometry and clarify its spatial relationship with aftershocks, we first determine focal mechanisms and relocate events with high precision. We utilize waveform data from over 300 stations in South Korea, equipped with broadband, short-period, and strong-motion sensors. Given the high station density in the epicentral region, we selected stations situated within about 100 km, ensuring optimal azimuthal coverage and good signal quality (see [Data and Resources](#)).

### Focal mechanisms

We constrain the focal mechanisms for the mainshock and three  $M_L \geq 2$  aftershocks (events 17, 29, and 38; Table 1). For the mainshock and event 17, we model waveforms and invert for focal mechanisms. The double-couple focal mechanism and seismic moment are determined through a grid search over strike, dip, and rake angles. Synthetics are calculated with a two-layer crustal velocity model for the KP ([Kim and Kim, 1983](#)), using the frequency-wavenumber integration method ([Saikia, 1994](#)). Both observed and synthetic waveforms are band-pass filtered between 0.03 and 0.1 Hz for the mainshock and 0.08–0.25 Hz for event 17. Focal depths are constrained by fitting the synthetics computed at 1 km depth

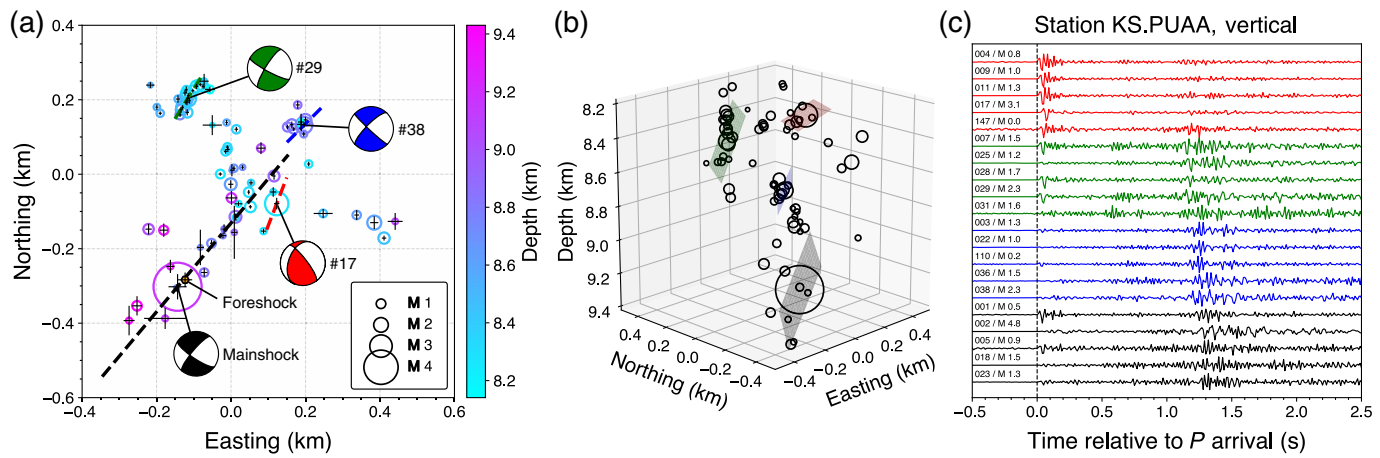
intervals and selecting the depth that minimizes waveform misfit (Fig. S1, available in the supplemental material to this article).

The  $M_w$  4.23 mainshock exhibits a strike-slip mechanism, with nodal planes striking northeast–southwest (NE–SW; 220°) and west-northwest–east-southeast (WNW–ESE; 124°), both with steep dips (~70°; Fig. S1a). The best-fitting focal depth is 9 ( $\pm 1$ ) km for the mainshock (Fig. S1a). Event 17, with  $M_w$  2.93, is the largest aftershock in the sequence and occurred about six hours after the mainshock. This event shows a thrust faulting mechanism (Fig. S1b). Its north-northeast-south-southwest (NNE–SSW; 201°)-trending nodal plane dips shallowly at 32°, whereas the NW–SE (322°)-trending nodal plane dips steeply at 72°. The best-fitting focal depth is 8 ( $\pm 1$ ) km, slightly shallower than the mainshock (Fig. S1b).

For the smaller events 29 and 38 (both  $M_w$  2.4), the low long-period energy precludes reliable waveform modeling. Instead, we rely on  $P$ -wave first motions to invert for the focal mechanism using FOCMEC (FOCal MEChanism determinations; [Snoke, 2003](#)).  $P$  polarity measurements with adequate azimuthal coverage enable focal mechanism solutions with high confidence (Fig. S1c). Both events show well-constrained strike-slip mechanisms with double-couple nodal planes oriented NE–SW and NW–SE, consistent with the mainshock. This suggests that events 29 and 38 likely ruptured on planar structures parallel to the mainshock, whereas event 17 occurred on a structurally distinct segment. The focal mechanisms of the four events are listed in Table 1.

### Fault geometry from the precise location of the earthquake sequence

To delineate the fault planes activated during the sequence, we locate earthquakes that occurred between 11 June 2024 and 20 March 2025. In addition to the 38 events reported by KMA, we apply a matched-filter technique to detect smaller events for which waveforms resemble those of template events cataloged by KMA. We detect 47 additional events with magnitudes ranging from -1.03 to 0.98 (Table S1). The magnitude of each detected event is estimated by measuring its peak amplitude



ratio relative to the best-matching template event, determined by the highest cross-correlation coefficient ( $C_c$ ).

Absolute locations are first determined using HYPOINVERSE (Klein, 2002) with manually picked  $P$ - and  $S$ -wave arrivals. Although the events are broadly distributed in the NE–SW direction, horizontal location uncertainties (0.1–1.4 km; Table S1) limit detailed geometric interpretation of the fault structure. Therefore, we refine the locations using the double-difference relocation code HypoDD (Waldhauser and Ellsworth, 2000). Differential travel times of  $P$  and  $S$  phases are measured by waveform cross correlation within a narrow time window of 0.1 s (from −0.03 to +0.07 s relative to  $P$  or  $S$  arrivals), after band-pass filtering between 2 and 25 Hz. We apply cutoff  $C_c$  thresholds of 0.8 for  $P$  and 0.9 for  $S$  phases, ultimately relocating a total of 74 events (Fig. 2a).

The relocated hypocenters, combined with focal mechanisms of  $M_L \geq 2$  events, reveal several clusters (i.e., fault segments; Fig. 2). A prominent NE–SW-trending seismicity at ~9 km depth aligns with the 220°-striking nodal plane of the mainshock. This cluster extends ~500 m both laterally and vertically (Fig. 2b). Notably, the location of the only foreshock (event 1) coincides with the mainshock hypocenter, possibly indicating a short-term nucleation process (e.g., Kim *et al.*, 2010; Gomberg, 2018). Event 38 ( $M_w$  2.4), which occurred eight months after the mainshock, is also aligned along the mainshock strike direction (Fig. 2a), but is offset by ~200 m when viewed from the depth section (Fig. 2b). Given its similar focal mechanism to the mainshock (Table 1), event 38 likely ruptured on a planar, shallower NE–SW-trending segment, hosting a cluster of closely spaced aftershocks.

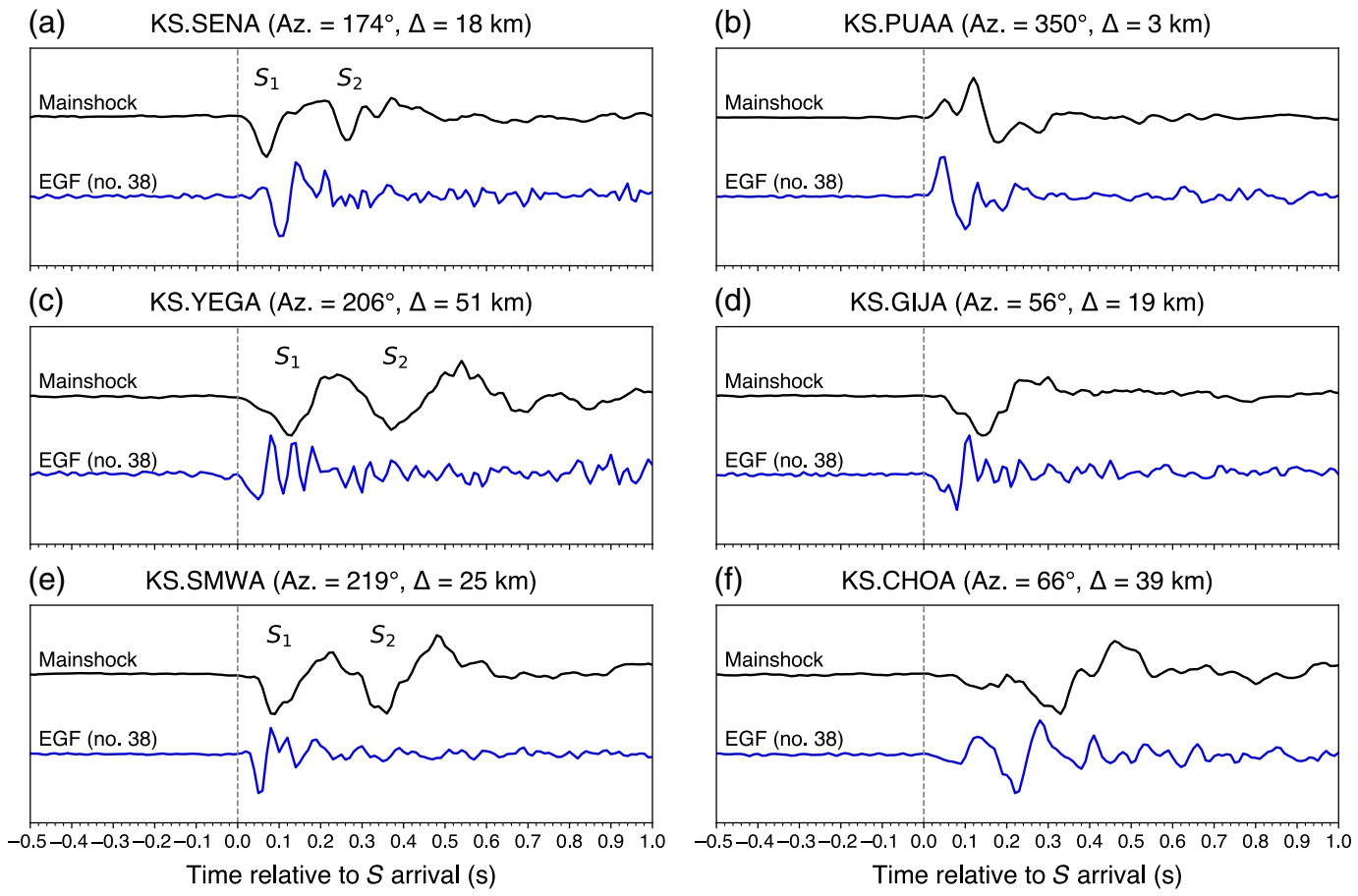
We identify two shallow, spatially distinct aftershock clusters associated with events 17 and 29. Their focal depths are ~1 km shallower than that of the mainshock, indicating that they occurred on isolated fault segments (Fig. 2b). A cluster near event 17 exhibits high-waveform similarities at the nearest station PUAA ( $\Delta = 3.4$  km, Az. = 350°), characterized by large  $P$ -to- $S$  amplitude ratios, suggesting consistent focal mechanisms (Fig. 2c). These events define a fault segment gently

**Figure 2.** (a) Map view of 74 earthquakes relocated using the double-difference algorithm. Events are color-coded by focal depth, with the foreshock marked by an orange hexagon. Event depths have been shifted relative to the mainshock depth determined by HYPOINVERSE (Table S1). Error bars correspond to 95% confidence intervals derived from the bootstrap resampling. Focal mechanisms of  $M \geq 2$  events are shown (Table 1), with inferred fault strikes indicated by colored dashed lines. Segmented fault planes of the mainshock, derived from the elliptical patch inversion (Table 2), are indicated by black-dashed lines. (b) Three-dimensional view of the relocated events and the fault planes associated with four  $M \geq 2$  events. Strike and dip angles of each plane are based on the focal mechanism solutions. (c) Unfiltered vertical-component waveforms recorded at station PUAA for five representative events, each selected from a different fault-plane cluster. Waveform colors correspond to the fault planes shown in panel (b). The color version of this figure is available only in the electronic edition.

dipping to the northwest, consistent with the NNE–SSW-trending nodal plane (strike = 201°) of event 17. Meanwhile, the cluster associated with event 29 clearly delineates a ~100-m-long NE–SW-trending subvertical segment, consistent with the 212°-striking nodal plane of event 29. Although event 29 ( $M_w$  2.4) is relatively small compared to the mainshock ( $M_w$  4.2) or event 17 ( $M_w$  2.9), this cluster is the most seismically productive during the sequence, possibly reflecting variations in fault properties or triggering mechanisms that influenced segment-specific seismicity.

## Mainshock Rupture Process

Observed  $S$  waves on transverse component records ( $SH$  phase) around the epicenter show azimuthal variation; in particular, the pulse duration of the  $SH$  phase varies with station azimuth as shown in Figure 3. For the stations located near the strike direction (220°) (Fig. 3a–c), the mainshock  $SH$  phases show notable complexity, for which a second pulse ( $S_2$ ) arrives 0.2–0.3 s after the first pulse ( $S_1$ ). However, this second pulse is absent in event 38, indicating that this feature is unlikely to be



path or site effects but rather reflects source-related complexity. On the other hand, for stations in the opposite directions (Fig. 3d–f), signals are much shorter and simpler, comparable to those of event 38. These observations suggest a complex source process involving rupture directivity. Such azimuthal variation has been observed for other moderate-sized earthquakes in the KP in recent years, including the 12 September 2016  $M_w$  5.4 Gyeongju earthquake in southeastern Korea (Uchide and Song, 2018) and the 16 December 2021  $M_w$  4.9 offshore Jeju Island earthquake (Han, Kim, Lim, et al., 2024). Boatwright (2007) also reported directivity in small earthquakes ( $3.5 < M < 4.1$ ) in San Ramon, California.

To unravel the complexity of the source, we employ a method for kinematic inversion of the rupture process based on the elliptical subfault approximation developed by Vallée and Bouchon (2004). They applied their method to two well-known large earthquakes ( $M_w > 7$ ) using teleseismic body and surface waves to determine the main features of the earthquake rupture in terms of one- and two-patch models. Di Carli et al. (2010) and Twardzik et al. (2012) employed the method for large earthquakes (2000  $M_w$  6.7, Tottori, Japan; 2004  $M_w$  6.0, Parkfield, California) using near-field strong-motion records.

In this study, we employ the same method for the moderate-size 2024  $M_w$  4.2 Buan earthquake, utilizing the empirical Green's function (EGF) approach to eliminate path and site

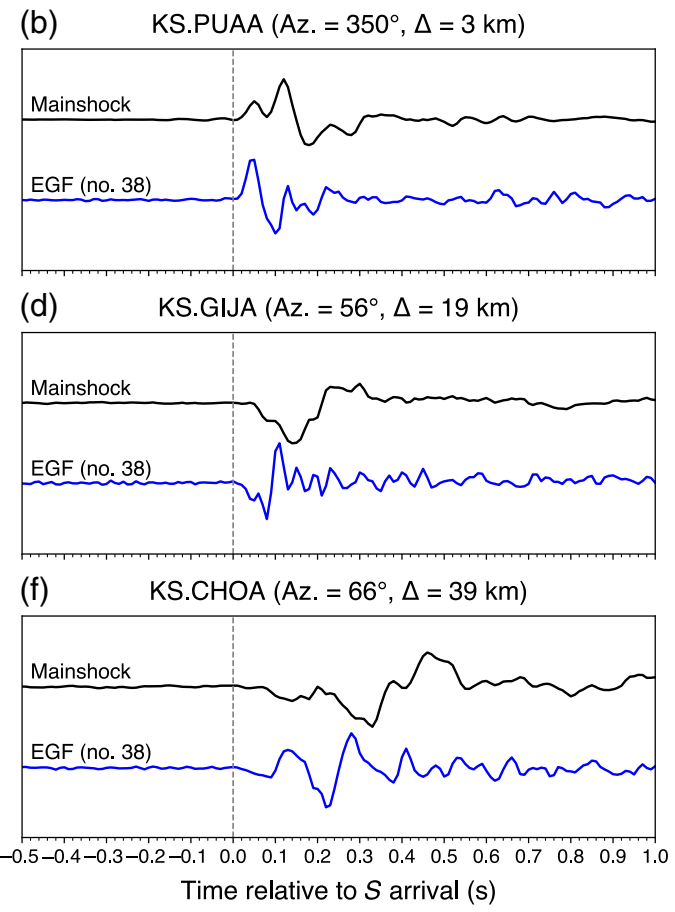
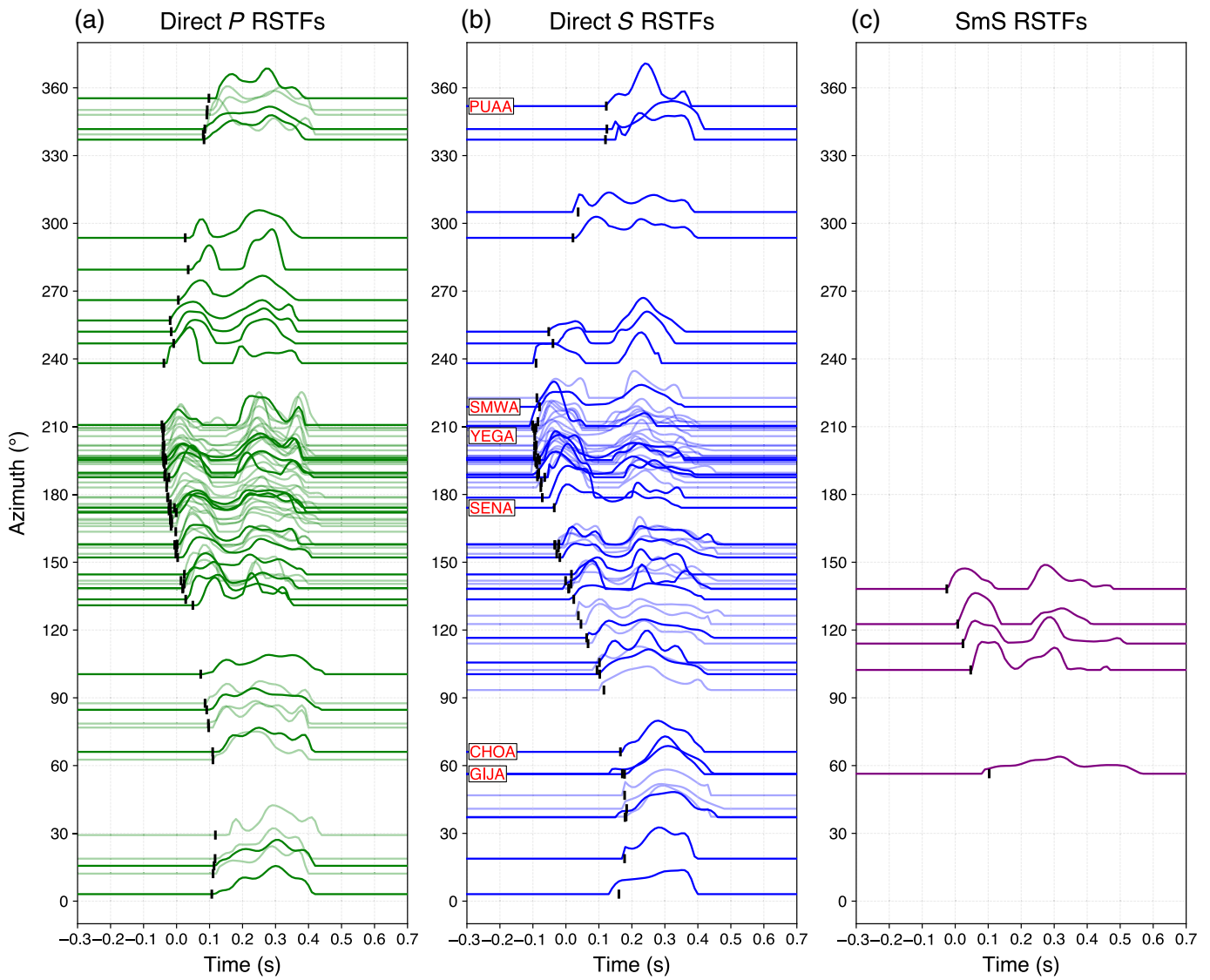


**Figure 3.** High-pass filtered (1 Hz) transverse-component velocity waveforms for the mainshock (black) and empirical Green's function (EGF) events (blue) are shown for (a,c,e) forward-strike stations and (b,d,f) backward-strike stations. All waveforms are aligned at the S-wave arrival. For the forward-strike stations, two distinct subevent signals are annotated as  $S_1$  and  $S_2$ . Note that the  $S_2$  signal appears only in the mainshock waveforms at the forward-strike stations. The color version of this figure is available only in the electronic edition.

effects from the observed seismic records at local distances (up to  $\sim 100$  km). RSTFs retrieved from stations at various distances and azimuths are then used to retrieve the main features of the mainshock rupture.

#### RSTFs from EGF deconvolution

We employ the EGF method to retrieve the RSTFs of the mainshock (Mori and Frankel, 1990). Event 38 is selected as the EGF event, which is located  $\sim 600$  m northeast of the mainshock hypocenter (Fig. 2a) with a similar focal mechanism as the mainshock (Table 1). It also exhibits a sufficiently large signal-to-noise ratio at stations up to 100 km from the epicenter. Although other aftershocks were also tested as EGF candidates and yielded similar RSTFs (Fig. S2), event 38 produced the most RSTFs that satisfied the quality criteria.

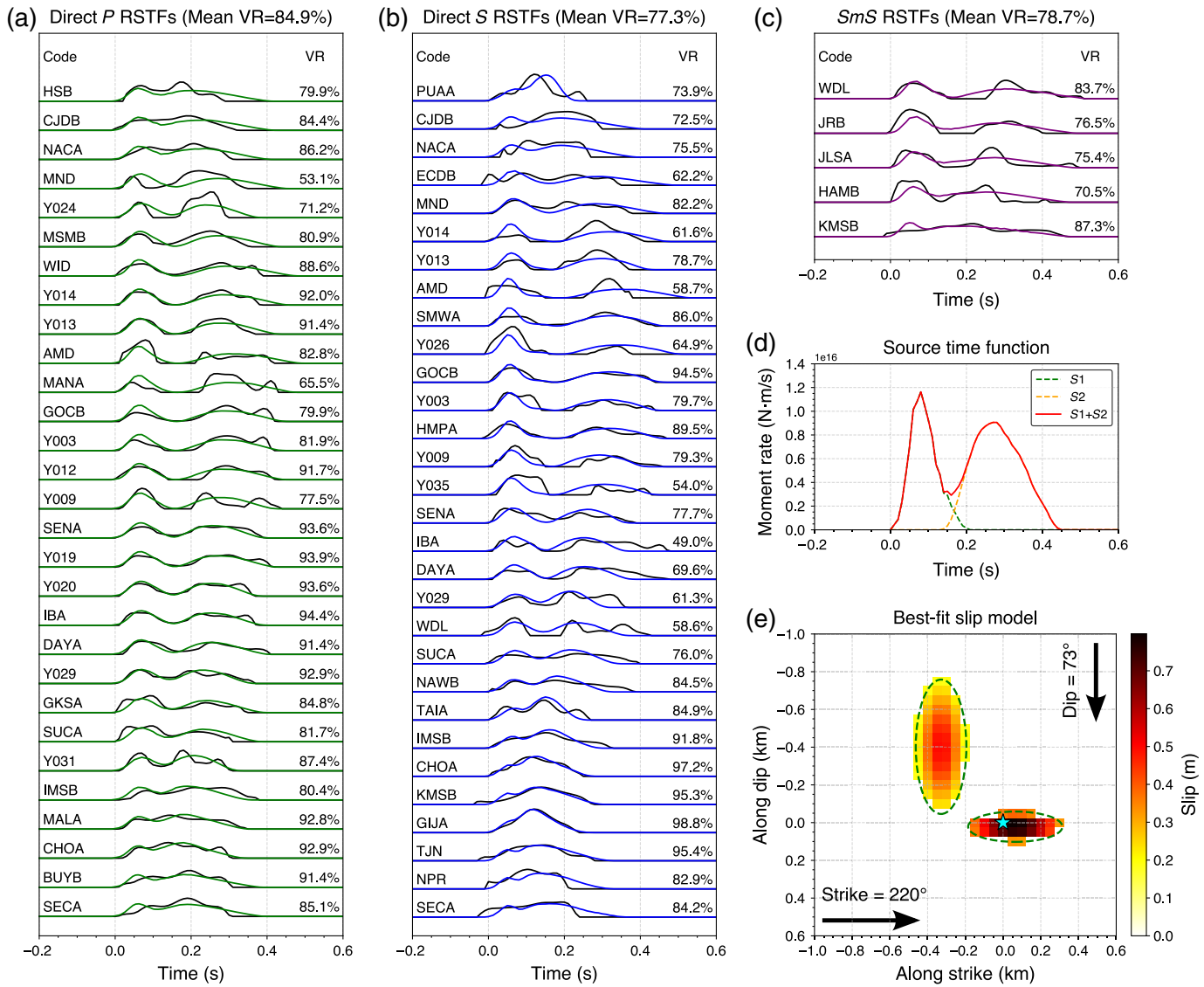


We follow the method of Han, Kim, Lim, *et al.* (2024) to retrieve the RSTF with waveforms windowed from 0.5 s before to 1.0 s after the *P* or *S* arrivals, and filtered at 1–10 Hz prior to deconvolution. The mainshock and EGF waveforms are aligned within a common time window starting from origin times. The projected Landweber deconvolution method with positivity and causality constraints is applied (Bertero *et al.*, 1997; Lanza *et al.*, 1999). In addition to direct *P* and *S* phases, we utilize the Moho-reflected *S* phase (*SmS*) at five stations at distances of 70–100 km. The use of *SmS* phase for source analysis was suggested by Song and Helmberger (1996) and Saikia and Helmberger (1997), but has been rarely used. Incorporating *SmS* RSTFs can enhance the resolution of the rupture model because the direct phases are primarily upgoing, whereas the *SmS* phases are downgoing from the source.

To ensure good-quality RSTFs, we require the variance reduction (VR) between the observed and synthetics—obtained by convolving the EGF with the RSTF—to exceed 70% (e.g., Meng *et al.*, 2020; Fig. S3). We further exclude

**Figure 4.** Relative source time functions (RSTFs) obtained from the mainshock–EGF pair for (a) direct *P*, (b) direct *S*, and (c) *SmS* phases that meet the quality criteria. The RSTFs are aligned by station azimuth and normalized by seismic moment. Those selected for constructing the slip model are shown with dark-colored lines, whereas others are shown with light-colored lines. Black vertical bars mark theoretical differential times, calculated based on the relative location between the mainshock and the EGF event. The RSTFs for stations shown in Figure 3 are annotated. The color version of this figure is available only in the electronic edition.

RSTFs from stations near radiation nodes of *P* and *SH* phases. After quality control, we obtain RSTFs from 73 *P*, 65 *SH*, and 5 *SmS* phases as plotted in Figure 4. The RSTFs show systematic azimuthal variations in start time and duration. The sinusoidal start-time variations reflect differences in hypocentral locations. The variations in duration indicate typical rupture directivity, with rupture propagating toward the northeast (~40°) and exhibiting shorter durations, whereas durations are longer



in the rear (southwest,  $\sim 220^\circ$ ). The inferred rupture direction is consistent with the NE–SW-striking nodal plane of the mainshock focal mechanism and the trend of the aftershock distribution (Fig. 2). In addition, the RSTFs from stations along the azimuth of  $\sim 120^\circ$  start to show a second source pulse, which persists up to  $\sim 300^\circ$  (Fig. 4). This indicates a rupture involving at least two subevents and suggests a complex rupture process of the mainshock.

### Mainshock rupture modeling: Elliptical subfault inversion

Motivated by the observation of double-pulse RSTFs at stations with azimuths between  $120^\circ$  and  $300^\circ$  (Fig. 4), we explore a kinematic rupture model composed of two elliptical patches to fit the RSTFs (Vallée and Bouchon, 2004). Although we have high-quality RSTFs with adequate station coverage (Fig. 1b), the distribution is uneven due to the offshore region in the west and high station density in the south. To mitigate potential bias in rupture modeling from this uneven spatial distribution, we

**Figure 5.** Comparisons between observed and synthetic apparent STFs (ASTFs) forward modeled from the best-fit elliptical patch model, shown for (a) direct  $P$ , (b) direct  $S$ , and (c)  $SmS$  phases. All ASTFs are aligned at their origin times ( $t = 0.0$  s) and normalized by seismic moment. Variance reductions (VRs) between observed and synthetic ASTFs at individual stations are indicated. (d) Source time function representing the overall rupture process. Contributions from the first patch ( $S_1$ ) and second patch ( $S_2$ ) are plotted as green and yellow dashed lines, respectively. (e) The best-fit two elliptical patch model plotted on the mainshock fault plane. The cyan star denotes the hypocenter. The color version of this figure is available only in the electronic edition.

bin the RSTFs into  $15^\circ$  intervals of azimuth ( $0^\circ$ – $360^\circ$ ) and take-off angle ( $45^\circ$ – $165^\circ$ ), resulting in 29, 30, and 5 groups for  $P$ ,  $SH$ , and  $SmS$  phases, respectively. From each group, we select the RSTF with the highest VR for inversion.

We assume that the final slip distribution can be represented as a combination of two elliptical patches. We then

TABLE 2  
**Summary of the Elliptical Patch Model for the Mainshock**

| <b>Model Parameter</b> | <b><math>a_1</math> (km)</b> | <b><math>b_1</math> (km)</b> | <b><math>x_1</math> (km)</b> | <b><math>y_1</math> (km)</b> | <b><math>a_2</math> (km)</b> | <b><math>b_2</math> (km)</b> | <b><math>x_2</math> (km)</b> | <b><math>y_2</math> (km)</b> | <b><math>s_1^{\max}/s_2^{\max}</math></b> | <b><math>V_r</math> (km/s)</b> |
|------------------------|------------------------------|------------------------------|------------------------------|------------------------------|------------------------------|------------------------------|------------------------------|------------------------------|---|--------------------------------|
| Best-fit value         | 0.250                        | 0.080                        | 0.065                        | 0.022                        | 0.134                        | 0.356                        | -0.329                       | -0.402                       | 1.687                                     | 2.176                          |
| Uncertainty range*     | (0.128, 0.341)               | (0.038, 0.180)               | (-0.016, 0.114)              | (-0.038, 0.061)              | (0.072, 0.273)               | (0.257, 0.433)               | (-0.417, -0.283)             | (-0.417, -0.283)             | (1.250, 2.414)                            | (2.088, 2.429)                 |

\*The uncertainty range denotes the minimum and maximum values for each model parameter such that the misfit is less than 1.1 times the global minimum misfit.

search for the optimal sizes and locations of the two ellipses by forward modeling synthetic apparent STFs (ASTFs) that best match the observed RSTFs. In detail, we search for 10 parameters, which are the centers ( $x_1, y_1; x_2, y_2$ ) and the major and minor axes of the two ellipses ( $a_1, b_1; a_2, b_2$ ), the ratio of maximum slip of the two patches ( $s_1^{\max}/s_2^{\max}$ ), and the rupture speed ( $V_r$ ). Within each ellipse, the slip distribution is assumed to follow a Gaussian distribution  $s(x, y) = s^{\max} \exp[-(\frac{x^2}{a^2} + \frac{y^2}{b^2})]$ . Moreover, we assume that the major and minor axes of the ellipses are parallel to the strike and dip of the fault plane. The rupture front is assumed to propagate from the hypocenter at a constant speed.

To forward model the RSTFs, one needs to specify the subfault grid size as well as the duration of the triangular slip-rate function corresponding to each subfault (or rise time  $t_r$ ). The grid size is set to 50 m in both strike and dip directions, and  $t_r$  is set to 0.06 s based on the empirical scaling relationship derived by Somerville *et al.* (1999). We test the sensitivity of both the grid size and  $t_r$  on the solution and find that the best-fit solution is robust to variations in these parameters (see Fig. S4).

The best-fit model is searched via the neighborhood algorithm (NA; Sambridge, 1999), which allows an efficient search in the high-dimensional model space through Voronoi cell partitioning. Although NA does not guarantee exhaustive sampling as a full grid search would, it has been successfully applied in a variety of rupture modeling studies (e.g., Vallée and Bouchon, 2004; Twardzik *et al.*, 2012). Moreover, NA generates an ensemble of solutions with comparable misfits, enabling uncertainty quantification. The misfit between synthetic and observed RSTFs is defined as the sum of least-squares misfits for direct  $P$ , direct  $S$ , and  $SmS$  phases:  $\sum_j [\sum_i^1 \sum_{N_j}^{N_j} \frac{\|obs_i - syn_i\|^2}{\|obs_i\|^2}]$ , in which  $i$  and  $j$  index stations and phases, respectively. The misfit definition enables better modeling of the relatively few  $SmS$  RSTFs, while maintaining good fits to the direct phases.

The best-fit model successfully reproduces the observed azimuthal variations in RSTF shape and duration, with average VRs of 84.9%, 77.3%, and 78.7% for direct  $P$ , direct  $S$ , and  $SmS$  phases, respectively (Fig. 5a–c). The final average source time function exhibits two distinct pulses in moment rate, spanning ~0.45 s (Fig. 5d). The model includes two clearly separated slip patches in which the first patch ( $S_1$ ) is located near

the hypocenter, whereas the second patch ( $S_2$ ) is located in the northeast, up-dip direction (Fig. 5e). The distance between the two patches is ~100 m. To estimate uncertainties of the model parameters, we select an ensemble of models with misfits less than 1.1 times the global minimum. Uncertainty bounds for each model parameter are given by their minimum and maximum values in Table 2.

### Linear slip inversion

To cross-validate the results from the elliptical subfault inversion, we perform a linear slip inversion following the approach of Dreger (1994). This approach models the apparent RSTFs using a 2D rupture propagating on a predefined fault plane at a constant rupture speed. We use 50 m × 50 m subfaults, consistent with the elliptical inversion. Considering the small number of available  $SmS$  RSTFs, we apply a weighting factor of six to the  $SmS$  phases relative to  $P$  and  $S$  phases, following the same weighting scheme used in the elliptical inversion. A nonnegative least-squares inversion is performed for each  $V_r$  and  $t_r$  pair, and the optimal combination is selected based on the maximum VR. The regularization parameter is set to  $\lambda = 500$  based on  $L$ -curve analysis (Mendoza and Hartzell, 2013). The optimal rupture model yields  $V_r = 0.62V_S$  and  $t_r = 0.05$  s. The resulting slip distribution shows two high-slip regions that are spatially correlated with the elliptical patches in the two-patch model (Fig. 6). The higher VR achieved in this model compared to the elliptical inversion likely reflects the greater modeling flexibility afforded by the unconstrained linear model (see Fig. S5). However, relatively weak slip patches observed in peripheral subfaults may be poorly resolved, possibly due to non-uniqueness inherent in the inversion process (Beresnev, 2003; Pennington, Uchide, and Chen, 2022).

An anticorrelation between high-slip regions and on-fault aftershock density is commonly observed in finite-fault inversion studies (e.g., Wössner *et al.*, 2006; Ross *et al.*, 2017), and is also evident in our case. Aftershocks within 100 m of the mainshock fault tend to cluster near the edges of the high-slip patches (Fig. 6), possibly indicating failure of unbroken barriers due to elevated coseismic stress (Das and Henry, 2003). Notably, some aftershocks also occurred between the two slip patches, which would be difficult to reconcile if the mainshock had ruptured a single large, continuous fault area.

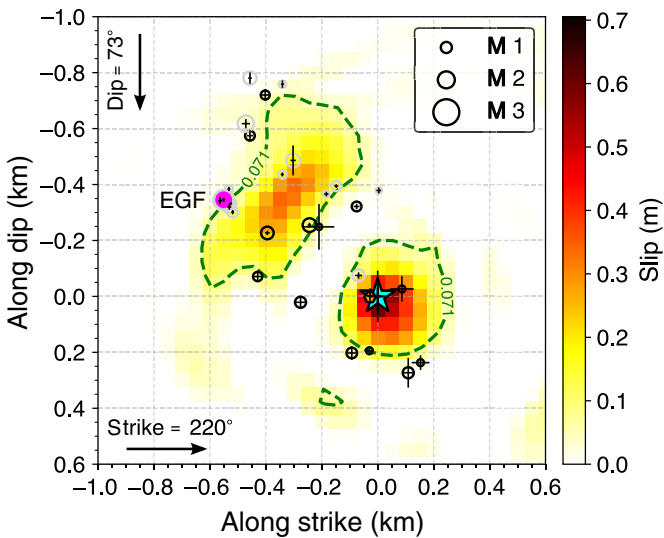


**Figure 6.** Slip distribution from the linear inversion. Contours indicating 10% of the peak slip are shown as green-dashed lines. The mainshock hypocenter (cyan star), foreshock (orange hexagon), and near-fault aftershocks (open circles) are projected onto the mainshock fault plane. The EGF event (event 38) is shown as a filled-magenta circle. Black circles represent aftershocks within 100 m of the mainshock fault, whereas gray circles denote those within 300 m. Error bars represent 95% confidence intervals derived from bootstrap resampling. The color version of this figure is available only in the electronic edition.

## Discussion

### Robustness and limitations of the two-patch rupture model

The key feature of the mainshock rupture process revealed by our analysis is substantial slip on two spatially distinct patches that ruptured sequentially, with a short-temporal overlap of approximately 0.05 s (Fig. 5d,e). Although we cannot exclude the possibility that a small amount of slip exists between the two patches—potentially forming a connecting zone not captured in the elliptical subfault inversion—the linear inversion, which imposes no assumptions about the number of patches, also reveals two clearly separated high-slip regions (Fig. 6). This consistency implies that the spatial separation between the two slip patches is likely a well-resolved and robust feature of the rupture model. We further attempted to model the RSTFs using three elliptical patches by adding an additional patch and found that the third patch is located within  $S_2$ , representing a localized high-slip region (Fig. S6). Although the average VR slightly improves, the third patch does not introduce a new rupture episode, supporting that the two-patch model sufficiently captures the essential features of the RSTF shapes.

In this study, we incorporate  $SmS$  phases alongside direct  $P$  and  $S$  phases to enhance rupture model resolution. To evaluate their contribution, we repeat both elliptical and linear inversions using only direct phase RSTFs. These inversions consistently

show that the second patch is poorly constrained (Fig. S7), indicating limited resolution in the dip direction when relying solely on phases with upgoing take-off angles. We also conduct inversions using only stations with 180° azimuthal coverage (Fig. S8), applying an aspect ratio penalty in the elliptical inversion to avoid overly elongated patches. In three out of four configurations, at least one  $SmS$  phase is included. We find that even with reduced azimuthal coverage, the relative positions of the two high-slip patches are reasonably recovered. However, excluding  $SmS$  phases causes the second patch to be poorly resolved in both size and location. Comparison of direct  $S$  and  $SmS$  RSTFs at azimuths 90°–150° (Fig. 4) shows that  $SmS$  RSTFs display double-pulse shapes with longer durations (~0.5 s), whereas direct  $S$  RSTFs are simpler and shorter (~0.3 to 0.4 s), reflecting the up-dip location and upward rupture propagation of  $S_2$ , captured by the different sensitivities of the upgoing ( $S$ ) and downgoing ( $SmS$ ) phases. These results demonstrate that  $SmS$  phases substantially improve rupture model resolution for small-to-moderate events, particularly under limited station coverage such as for offshore earthquakes. Other downgoing phases, such as  $PmP$  or  $Pn$ , could be explored in future studies to provide similar constraints.

In addition to slip distribution, we resolve a rupture speed of  $0.63V_S$  (Table 2), which is lower than the  $0.7$ – $0.8V_S$  typically reported for large global earthquakes (Geller, 1976; Vera et al., 2024), or the commonly assumed  $0.9V_S$  used in stress-drop estimation based on simple circular crack models (Madariaga, 1976). Guo et al. (2023) systematically investigated  $M_w \geq 6$  shallow strike-slip events and found that rupture speed correlates inversely with fault maturity. In this context, the slow rupture of the Buan event may similarly reflect rupture on an immature fault within a slowly deforming SCR (e.g., Pennington, Chang, et al., 2022; Žilić et al., 2025). However, the uncertainty range derived from our NA solution ensemble (0.60–0.70 $V_S$ ) indicates that a wide range of rupture speeds can also explain the observed RSTFs with similarly low misfits. Importantly, both the elliptical and linear inversions assume a constant rupture speed across the entire rupture. In other words, a single rupture speed is used to simultaneously match both the azimuthal variation in RSTF pulse widths and the azimuth-dependent timing of the two subevents. In reality, the rupture speed may vary significantly, as shown in dynamic rupture simulations (Li et al., 2023; Gallovič et al., 2025). Given the short-rupture duration (~0.45 s; Fig. 5d) and the inherent non-uniqueness of finite-source inversions, introducing a variable rupture speed is unlikely to yield meaningful improvements for this event.

### Complex rupture and high stress drop in a stable continental crust

To date, only a handful of earthquakes in the KP have been investigated with detailed rupture models (Abdel-Fattah et al., 2014; Uchide and Song, 2018; Cho et al., 2023; Han, Kim, Lim, et al., 2024). These studies suggest that complex ruptures may

be relatively common even among moderate-sized events in the region. For instance, [Han, Kim, Lim, et al. \(2024\)](#) used RSTF modeling to show that the 2021  $M_w$  4.9 offshore Jeju Island earthquake involved sequential rupture of two distinct slip patches over  $\sim$ 1.2 s. Interestingly, these two subevents were separated by a  $\sim$ 0.2 s pause, allowing us to constrain the rupture speeds of each patch. Their results revealed distinct rupture directivities and speeds between the patches, implying substantial heterogeneity in rupture dynamics along the short fault ( $\sim$ 2 km). Although the overall rupture duration of the 2024 Buan mainshock was much shorter, its rupture pattern closely resembles that of the 2021 Jeju Island earthquake. Specifically,  $S_1$  ruptured bilaterally with some asymmetry, whereas  $S_2$  propagated northeastward and up-dip (Fig. 6). A key difference is that in the 2024 Buan event,  $S_2$  followed  $S_1$  almost instantaneously, whereas in the 2021 Jeju event, the two subevents were separated by a  $\sim$ 0.2 s pause. This contrast in timing suggests different triggering mechanisms: although the Jeju event rupture may have involved static stress transfer between the two patches ([Ellsworth and Bulut, 2018](#); [Han, Kim, Lim, et al., 2024](#)), the short-temporal overlap ( $\sim$ 0.05 s) in the Buan event indicates that the second rupture began before the first had fully terminated. This close temporal overlap indicates a substantial role of transient dynamic stress in triggering  $S_2$ , although distinguishing contributions of dynamic and static stress changes remains challenging ([Belardinelli et al., 1999](#); [Antonioli et al., 2002](#)). Alternatively, the event may represent a single rupture episode, as the timing between patch failures is consistent with a reasonable rupture speed.

Another noteworthy feature of the Buan rupture model is the locally elevated stress drops in both slip patches. Using the analytical solution for elliptical cracks ([Eshelby, 1957](#); [Kaneko and Shearer, 2015](#)), we estimate the stress drop for each patch, with uncertainty bounds derived from the NA solution ensemble (Fig. S9a). Despite large uncertainties, the inferred stress drops are substantially high: 227 (74–741) MPa for  $S_1$  and 82 (20–270) MPa for  $S_2$ . These estimates show a strong positive correlation, which arises naturally from the positively correlated rupture areas of the two patches (Fig. S9b). Approximating the total rupture area using the minimum-area ellipse encompassing both patches, we obtain an average stress drop of  $\sim$ 15 MPa. Although this value is much lower than the stress drops of individual patches, it aligns well with previously reported average stress-drop estimates for other moderate-size earthquakes in the KP (e.g., [Kim et al., 2010](#); [Uchide and Song, 2018](#)).

Stress drops that are locally high but low on average have also been reported for M 2–4 earthquakes in Northern California using finite-fault modeling ([Dreger et al., 2007](#); [Taira et al., 2015](#)). Despite the contrasting tectonic environments, the 2016 Gyeongju earthquake sequence in southeastern Korea exhibited comparable behavior, with stress drops of up to 62 MPa for the mainshock ( $M_w$  5.4) and 43 MPa for the largest

foreshock ( $M_w$  5.0), whereas the average values were significantly lower at 23 and 15 MPa, respectively ([Uchide and Song, 2018](#)). The 2024 Buan earthquake also exhibited two spatially separated high-slip patches with locally elevated stress drops up to  $\sim$ 230 and  $\sim$ 80 MPa, whereas the average stress drop was rather low at  $\sim$ 15 MPa. These observations suggest that localized zones of high stress drop may not be limited to specific tectonic environments, but can occur in both active and stable crustal settings, thereby influencing rupture initiation and propagation ([Day et al., 1998](#); [Li et al., 2023](#)).

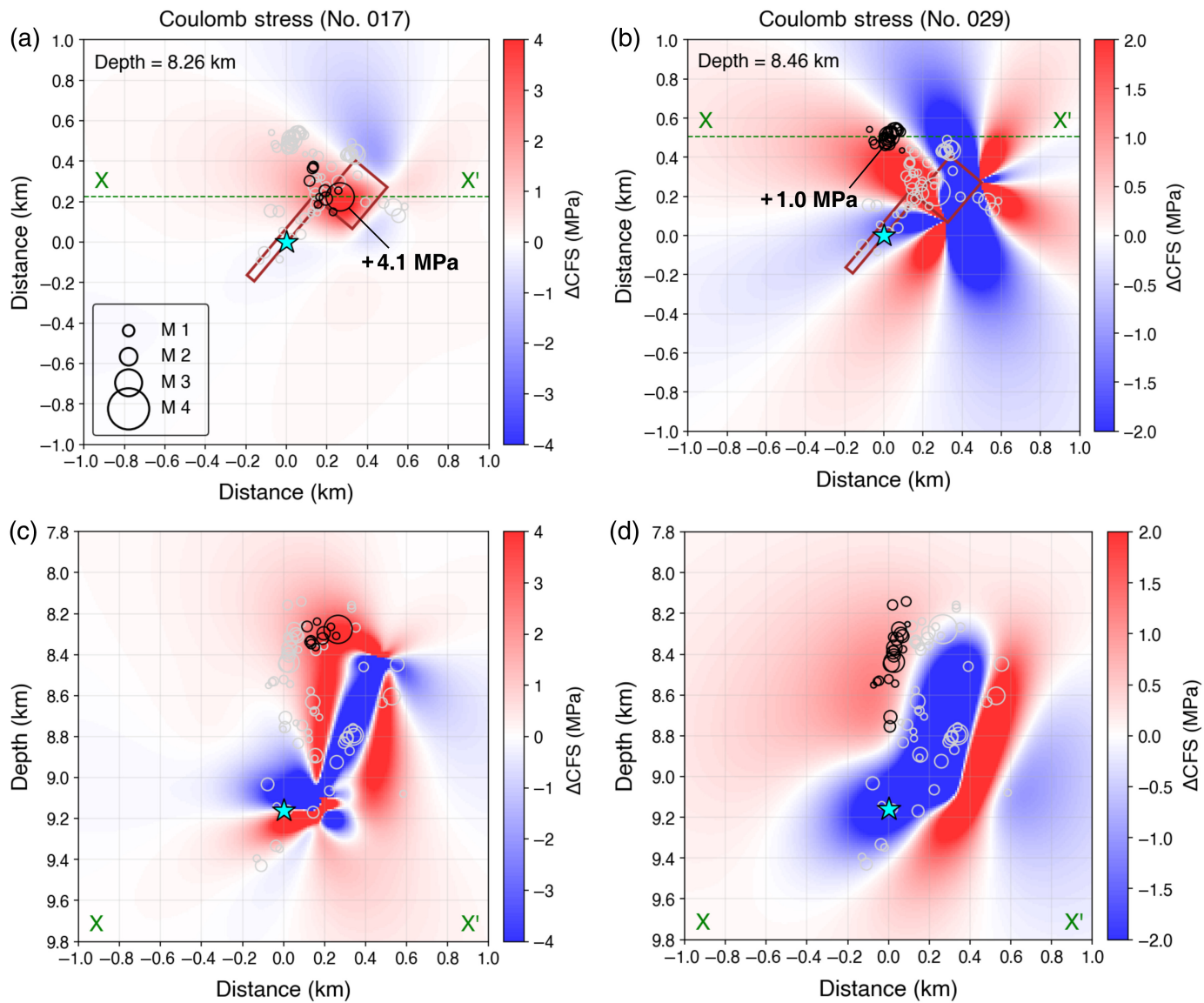
### Aftershock triggering in a complex fault network

The relocated 2024 Buan earthquake sequence reveals that at least two shallow and spatially distinct fault planes are activated during the sequence (Fig. 2b). The focal mechanisms of the largest events in each segment are well constrained (Table 1), which enables an assessment of whether these aftershocks were triggered by stress changes imparted by the mainshock rupture. We conduct Coulomb stress transfer analysis using the Coulomb 3.3 software ([Toda et al., 2011](#)). We first built the mainshock source model composed of two rectangular patches based on the best-fitting elliptical patch model (Table 2). We then calculate shear ( $\Delta\tau$ ) and normal ( $\Delta\sigma$ ) stress changes on the receiver fault planes (Fig. 7). The Coulomb failure stress change ( $\Delta\text{CFS}$ ) is then calculated as  $\Delta\text{CFS} = \Delta\tau + \mu\Delta\sigma$ , in which  $\mu$  is the effective friction coefficient. We assume a commonly adopted value of  $\mu = 0.6$  ([Soh et al., 2018](#)). A positive  $\Delta\text{CFS}$  on the receiver fault indicates that slip is promoted, whereas a negative  $\Delta\text{CFS}$  suggests that slip is inhibited.

For both events 17 and 29, we calculate the  $\Delta\text{CFS}$  imparted by the mainshock, assuming the NE–SW- or NNE–SSW-trending nodal planes as receiver faults. The results show clearly positive  $\Delta\text{CFS}$  values, which are +4.1 MPa for event 17 and +1.0 MPa for event 29 (Fig. 7). Aftershocks associated with each fault segment also exhibit good spatial correlation with regions of positive  $\Delta\text{CFS}$ , suggesting that seismicity on these structures was primarily influenced by the mainshock rupture, although secondary triggering by aftershocks cannot be ruled out ([Marsan and Lengline, 2008](#)). Notably, the down-dip extent of seismicity on the event 29 fault coincides with the boundary of the positive  $\Delta\text{CFS}$  region, suggesting that deeper seismicity may have been inhibited by the surrounding stress shadow zone (Fig. 7d). To test the robustness of our results against the choice of slip model, we repeat the calculations with the linear inversion slip model and find that the overall pattern is consistent (Fig. S10).

### Fault plane of the largest aftershock

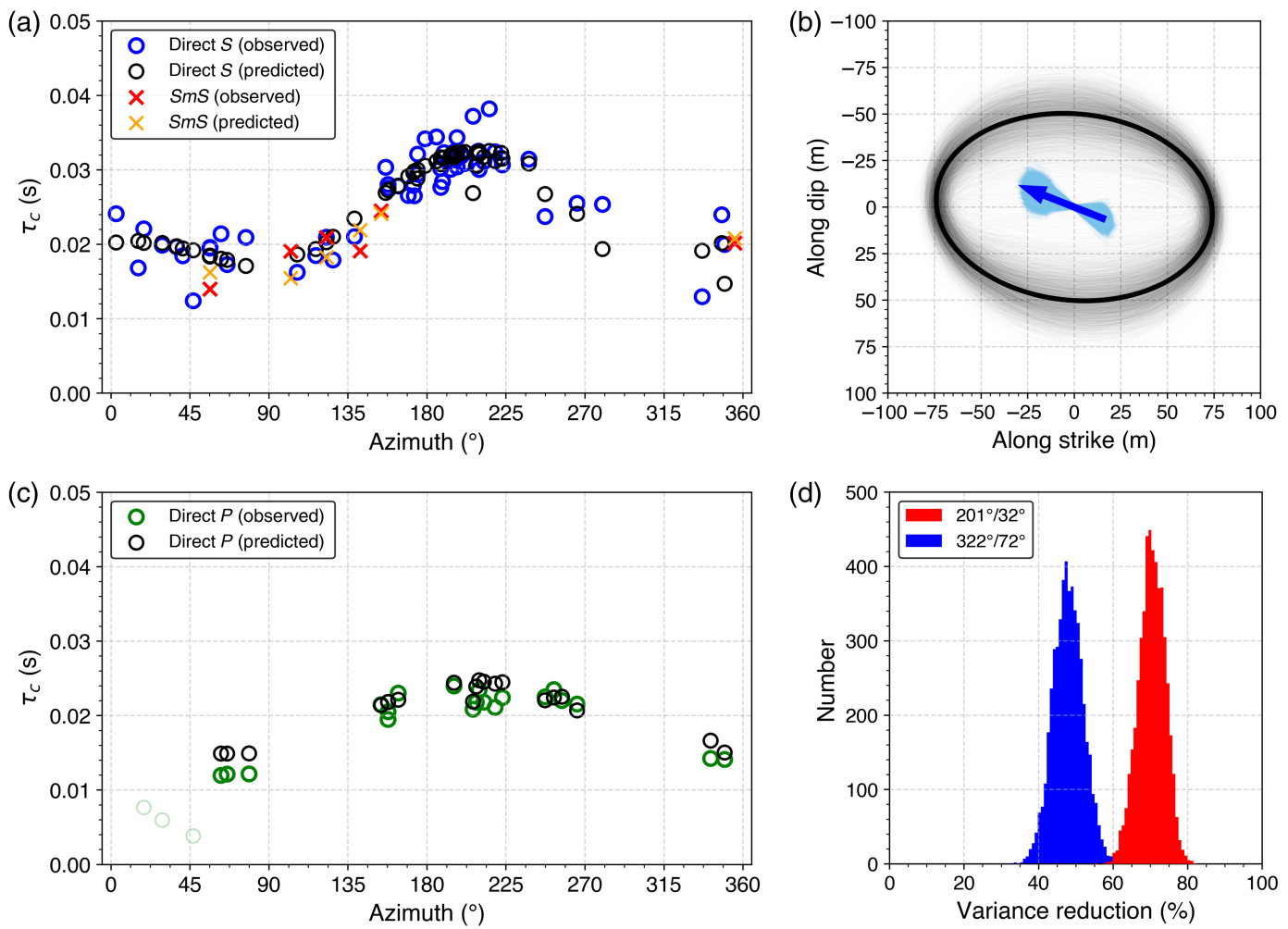
According to our relocation results (Fig. 2), the Buan earthquake sequence predominantly ruptured along NE–SW- or NNE–SSW-striking fault planes. However, the fault-plane geometry of the largest aftershock (event 17) remains uncertain, as the



spatial distribution of epicenters does not clearly delineate the strike direction, likely due to its pronounced reverse-faulting component. Han and Kim (2025), based on their independent relocation of events during the first two days of the Buan sequence, suggested that event 17 may have ruptured a NW–SE-striking fault. They further evaluated its rupture potential using a quasi-dynamic simulation based on rate-and-state friction and found that unrealistically low friction ( $\mu < 0.2$ ) would be required for rupture nucleation under the regional stress field.

To provide independent constraints on the fault-plane geometry, we analyze the rupture directivity and spatial extent of event 17 using the second-degree moment inversion approach (McGuire, 2004; Meng *et al.*, 2020; Guo *et al.*, 2025). This method has proven effective in resolving fault-plane ambiguities, particularly for small- to moderate-size earthquakes ( $M \leq 5$ ). Following the EGF deconvolution procedure applied to the mainshock (see the Mainshock rupture process section), we calculate RSTFs with  $VR \geq 70\%$  for the  $P$ ,  $S$ , and  $SmS$  phases. We

**Figure 7.** (a) Coulomb failure stress change ( $\Delta CFS$ ) calculated for the receiver fault of event 17, assuming (strike, dip, rake) = (201°, 32°, 144°) at 8.26 km depth. The input mainshock source model is shown as the brown rectangles, and the mainshock hypocenter is shown as a cyan star. Events associated with the target fault plane are shown as black circles, whereas other events are shown as gray circles. (b) Same as panel (a), but for the receiver fault of event 29, assuming (strike, dip, rake) = (212°, 73°, -166°) at 8.46 km depth. (c) Cross section of  $\Delta CFS$  along the X-X' line in panel (a). (d) Cross-section of  $\Delta CFS$  along the X-X' line in panel (b). The color version of this figure is available only in the electronic edition.



second-degree moment method. To ensure physically meaningful solutions (i.e., positive rupture duration and area), we formulate the inversion as a nonnegative least-squares problem and solve it using a convex optimization framework (Diamond and Boyd, 2016). We perform separate inversions for the two candidate nodal planes and select the one with the lower misfit as the preferred fault plane. To assess uncertainty and significance, we perform 5000 bootstrap inversions by adding Gaussian noise to the apparent  $\tau_c$  values, sampled from  $N(0, \sigma)$ , in which  $\sigma$  is the root-mean-square misfit of the original inversion.

The inversion strongly favors the NNE–SSW-oriented nodal plane as the actual fault plane, achieving a significantly higher VR (82%) compared to the NW–SE plane (55%). The close match between the predicted and observed  $\tau_c$  values (Fig. 8a,b) indicates that the solution is well constrained. The rupture dimension is approximately  $150\text{ m} \times 100\text{ m}$ , with rupture propagating dominantly toward an azimuth of  $\sim 40^{\circ}$  (Fig. 8c; Table S2). Furthermore, bootstrap results show consistently high-VR values for the NNE–SSW plane (Fig. 8d). Therefore, we interpret the NNE–SSW-trending nodal plane as the actual rupture plane for event 17.

**Figure 8.** (a) Characteristic durations ( $\tau_c$ ) from S-wave RSTFs plotted as a function of station azimuth. Observed values are shown as blue-open circles (direct S) and red crosses (SmS), whereas predicted durations are shown as black-open circles (direct S) and orange crosses (SmS). (b) Best-fitting second-moment ellipse (black), with semimajor and semi-minor axes representing  $L_c$  and  $W_c$ , and centroid directivity vector (blue arrow) scaled by  $v_0 \times \tau_c$ . Gray ellipses and light-blue arrows indicate the ensemble of solutions derived from 5000 inversions with added random noise. (c)  $\tau_c$  values from P-wave RSTFs plotted by azimuth. Observed and predicted durations for direct P phases are shown as green and black open circles, respectively. Light-colored open circles indicate measurements from very short RSTFs with limited resolution, which were excluded from the inversion. (d) Histograms of VRs for the two nodal planes, derived from the 5000 inversion ensembles with added random noise. The color version of this figure is available only in the electronic edition.

## Conclusions

We analyze the rupture process of the 2024  $M_w$  4.2 Buan earthquake by constructing a kinematic rupture model that consists of two elliptical patches using EGF-derived RSTFs. The model reveals a complex rupture involving two spatially distinct slip

patches that rupture sequentially with a short temporal overlap. The estimated stress drops for the two patches are locally high, approximately 230 and 80 MPa, whereas the average stress drop is about 15 MPa, consistent with estimates from previous moderate-size events in the southern KP. The rupture predominantly propagated in the northeastward and up-dip directions, consistent with the NE-SW alignment of the aftershocks. Both on- and off-fault aftershocks appear to have been triggered by stress transfer from the mainshock; on-fault aftershocks are located near the edges of the high-slip regions, whereas off-fault clusters coincide with areas of positive Coulomb stress changes. These findings demonstrate that even moderate-sized earthquakes in SCRs exhibit complex rupture processes, heterogeneous stress drops, and systematic aftershock triggering governed by fault geometry and stress interaction.

## Data and Resources

Waveform data of the Korea Meteorological Administration (KMA) were downloaded from the National Earthquake Comprehensive Information System website (<https://necis.kma.go.kr>) upon registration; data from the Korea Institute of Geoscience and Mineral Resources (KIGAM) are accessible from the Geo Big Data Open Platform of KIGAM (<https://data.kigam.re.kr/quake/data>) upon registration; data of the Korea Institute of Nuclear Safety were acquired through personal communication and are not publicly accessible. Seismic data were processed using the Seismic Analysis Code (SAC) version 101.6a (<https://ds.iris.edu/ds/nodes/dmc/software/downloads/sac/>; Goldstein and Snoker, 2005) and ObsPy version 1.4.0 (<https://docs.obspy.org/archive/1.4.0/>; Beyreuther *et al.*, 2010). First-motion focal mechanisms were determined using FOCMEC (<http://ds.iris.edu/pub/programs/focmec/>; Snoker, 2003). Absolute earthquake locations were determined using HYPOINVERSE-2000 (<https://www.usgs.gov/software/hypoinverse-earthquake-location>; Klein, 2002), and double-difference relocations were performed using HypoDD version 1.3 (~<https://www.ldeo.columbia.edu/~felixw/hypoDD.html>; Waldhauser and Ellsworth, 2000). The neighborhood algorithm (NA) was implemented using the Python library neighpy (<https://neighpy.readthedocs.io/en/latest>). Coulomb stress analysis was conducted using Coulomb 3.3 software (<https://temblor.net/coulomb/>; Toda *et al.*, 2011). Second moment inversion analysis was conducted based on a Python script modified from an openly available MATLAB toolbox ([https://www.seismosoc.org/Publications/SRL/SRL\\_88/srl\\_88-2A\\_mcguire-esupp/](https://www.seismosoc.org/Publications/SRL/SRL_88/srl_88-2A_mcguire-esupp/); McGuire, 2017). Figures were created using Matplotlib version 3.7.1 (<https://matplotlib.org/3.7.1>; Hunter, 2007) and Inkscape version 1.1 (<https://inkscape.org/release/inkscape-1.1>). Maps were created using PyGMT version 0.10.0 (<https://www.pygmt.org/v0.10.0/>; Uieda *et al.*, 2021), a Python library based on Generic Mapping Tools (GMT) version 6 (<https://www.generic-mapping-tools.org/>; Wessel *et al.*, 2019). Codes used for performing rupture modeling are available from the corresponding author upon request. All websites were last accessed in July 2025. The supplemental material for this article includes 11 figures and 2 tables.

## Declaration of Competing Interests

The authors acknowledge that there are no conflicts of interest recorded.

## Acknowledgments

This research was supported by the Korea Meteorological Administration (KMA) Research and Development Program (Grant Number RS-2025-02313103) and the National Research Foundation (NRF) of Korea (Grant Number RS-2022-NR070842). W.-Y. Kim also acknowledges support from the Brain Pool Program through the NRF, funded by the Ministry of Science and ICT through the NRF of Korea (Grant Number RS-2024-00444848). Authors acknowledge the Korea Institute of Nuclear Safety for granting permission to use the waveform data. The authors thank the editor and the associate editor for support to this work, and appreciate two anonymous reviewers for their constructive comments.

## References

- Abdel-Fattah, A. K., K. Y. Kim, M. S. Fnais, and A. M. Al-Amri (2014). Source process and tectonic implication of the January 20, 2007 Odaesan earthquake, South Korea, *Phys. Earth Planet. In.* **229**, 72–81, doi: [10.1016/j.pepi.2014.01.006](https://doi.org/10.1016/j.pepi.2014.01.006).
- Antonioli, A. M., S. D. Cocco, and C. Henry (2002). Dynamic stress triggering during the great 25 March 1998 Antarctic Plate earthquake, *Bull. Seismol. Soc. Am.* **92**, no. 3, 896–903.
- Beaucé, E., F. Waldhauser, D. Schaff, W.-Y. Kim, and F. Kolawole (2025). The 5 April 2024  $M_w$  4.8 Tewksbury, New Jersey aftershock sequence resolved with machine-learning-enhanced detection methods, *Geophys. Res. Lett.* **52**, no. 12, doi: [10.1029/2024GL113598](https://doi.org/10.1029/2024GL113598).
- Belardinelli, M. E., M. Cocco, O. Coutant, and F. Cotton (1999). Redistribution of dynamic stress during coseismic ruptures: Evidence for fault interaction and earthquake triggering, *J. Geophys. Res.* **104**, no. B7, 14,925–14,945.
- Beresnev, I. A. (2003). Uncertainties in finite-fault slip inversions: To what extent to believe? (a critical review), *Bull. Seismol. Soc. Am.* **93**, no. 6, 2445–2458.
- Bertero, M., D. Bindi, P. Boccacci, M. Cattaneo, C. Eva, and V. Lanza (1997). Application of the projected Landweber method to the estimation of the source time function in seismology, *Inverse Probl.* **13**, no. 2, 465–486.
- Beyreuther, M., R. Barsch, L. Krischer, T. Megies, Y. Behr, and J. Wassermann (2010). ObsPy: A Python toolbox for seismology, *Seismol. Res. Lett.* **81**, no. 3, 530–533.
- Boatwright, J. (2007). The persistence of directivity in small earthquakes, *Bull. Seismol. Soc. Am.* **97**, no. 6, 1850–1861.
- Boyd, O. S., D. E. McNamara, S. Hartzell, and G. Choy (2017). Influence of lithostatic stress on earthquake stress drops in North America, *Bull. Seismol. Soc. Am.* **107**, no. 2, 856–868.
- Chapman, M. C. (2013). On the rupture process of the 23 August 2011 Virginia earthquake, *Bull. Seismol. Soc. Am.* **103**, no. 2A, 613–628.
- Cho, E., J.-U. Woo, J. Rhie, T.-S. Kang, and S. Y. Baag (2023). Rupture process of the 2017  $M_w$  5.5 Pohang, South Korea, Earthquake via an Empirical Green's function method, *Bull. Seismol. Soc. Am.* **113**, no. 2, 592–603.
- Das, S., and C. Henry (2003). Spatial relation between main earthquake slip and its aftershock distribution, *Rev. Geophys.* **41**, no. 3, doi: [10.1029/2002RG000119](https://doi.org/10.1029/2002RG000119).
- Day, S. M., G. Yu, and D. J. Wald (1998). Dynamic stress changes during earthquake rupture, *Bull. Seismol. Soc. Am.* **88**, no. 2, 512–522.
- Di Carli, S., C. François-Holden, S. Peyrat, and R. Madariaga (2010). Dynamic inversion of the 2000 Tottori earthquake based on

- elliptical subfault approximations, *J. Geophys. Res.* **115**, no. B12, doi: [10.1029/2009JB006358](https://doi.org/10.1029/2009JB006358).
- Diamond, S., and S. Boyd (2016). CVXPY: A Python-embedded modeling language for convex optimization, *J. Mach. Learn. Res.* **17**, no. 83, 1–5.
- Dreger, D., R. M. Nadeau, and A. Chung (2007). Repeating earthquake finite source models: Strong asperities revealed on the San Andreas Fault, *Geophys. Res. Lett.* **34**, no. 23, doi: [10.1029/2007GL031353](https://doi.org/10.1029/2007GL031353).
- Dreger, D. S. (1994). Empirical Green's function study of the January 17, 1994 Northridge, California earthquake, *Geophys. Res. Lett.* **21**, no. 24, 2633–2636.
- Ellsworth, W. L., and F. Bulut (2018). Nucleation of the 1999 Izmit earthquake by a triggered cascade of foreshocks, *Nat. Geosci.* **11**, no. 7, 531–535.
- Eshelby, J. D. (1957). The determination of the elastic field of an ellipsoidal inclusion, and related problems, *Proc. Math. Phys. Sci.* **241**, no. 1226, 376–396.
- Gallovič, F., V. Plicka, L. Valentová, E. Sokos, and J. Zahradník (2025). Complex dynamic rupture of an  $M_w$  5.8 intermediate-depth earthquake in the Hellenic slab, *Geophys. Res. Lett.* **52**, no. 7, doi: [10.1029/2024GL113649](https://doi.org/10.1029/2024GL113649).
- Geller, R. J. (1976). Scaling relations for earthquake source parameters and magnitudes, *Bull. Seismol. Soc. Am.* **66**, no. 5, 1501–1523.
- Godano, M., C. Larroque, B. Delouis, J.-P. Ampuero, F. Arzu, F. Courboulex, A. Deschamps, M. van den Ende, S. Baize, and J.-F. Ritz (2025). Back to the source: Connecting the seismological observations of Le Teil earthquake ( $M_w$  4.9, 2019/11/11, France) to the local geology, *J. Geophys. Res.* **130**, no. 9, doi: [10.1029/2025JB031133](https://doi.org/10.1029/2025JB031133).
- Goldstein, P. A. U. L., and A. Snoke (2005). SAC availability for the IRIS community, *Incorporated Research Institutions for Seismology Data Management Center Electronic Newsletter*, available at <https://seiscode.iris.washington.edu/projects/sac> (last accessed August 2025).
- Gomberg, J. (2018). Unsettled earthquake nucleation, *Nat. Geosci.* **11**, no. 7, 463–464.
- Guo, H., J. W. Atterholt, J. J. McGuire, and C. Thurber (2025). Evidence for low effective stress within the crust of the subducted Gorda plate from the 2022 December  $M_w$  6.4 Ferndale earthquake sequence, *Seismol. Res. Lett.* **96**, no. 3, 1504–1520.
- Guo, H., T. Lay, and E. E. Brodsky (2023). Seismological indicators of geologically inferred fault maturity, *J. Geophys. Res.* **128**, no. 10, doi: [10.1029/2023JB027096](https://doi.org/10.1029/2023JB027096).
- Han, J., and S. Kim (2025). The 2024  $M_L$  4.8 Buan earthquake sequence and aligned multiple clusters in the southwestern Korean Peninsula, *Geosci. J.* 1–15, doi: [10.1007/s12303-025-00048-x](https://doi.org/10.1007/s12303-025-00048-x).
- Han, S., W.-Y. Kim, H. Lim, Y. O. Son, M.-S. Seo, J. Y. Park, and Y. Kim (2024). Resolving multi-stage rupture process of the 2021  $M_w$  4.9 Offshore Jeju Island earthquake from relative source time functions, *Geophys. Res. Lett.* **51**, no. 3, doi: [10.1029/2023GL106059](https://doi.org/10.1029/2023GL106059).
- Han, S., W.-Y. Kim, J. Y. Park, M.-S. Seo, and Y. Kim (2024). Rupture Model of the 5 April 2024 Tewksbury, New Jersey, earthquake based on regional Lg-wave data, *Seism. Record* **4**, no. 3, 214–222.
- Hartzell, S., C. Mendoza, and Y. Zeng (2013). Rupture model of the 2011 Mineral, Virginia, earthquake from teleseismic and regional waveforms, *Geophys. Res. Lett.* **40**, no. 21, 5665–5670.
- Horton, J. W., M. C. Chapman, and R. A. Green (2015). The 2011 Mineral, Virginia, earthquake, and its significance for seismic hazards in eastern North America— Overview and synthesis, in *The 2011 Mineral, Virginia, Earthquake, and its Significance for Seismic Hazards in Eastern North America*, M. Horton Jr., C. Chapman, and R. A. Green (Editors), Geological Society of America, Boulder, Colorado, Special Paper 509, 1–25, doi: [10.1130/2015.2509\(01\)](https://doi.org/10.1130/2015.2509(01)).
- Hunter, J. D. (2007). Matplotlib: A 2D graphics environment, *Comput. Sci. Eng.* **9**, no. 03, 90–95.
- Jin, S., Z. C. Li, and P. H. Park (2006). Seismicity and GPS constraints on crustal deformation in the southern part of the Korean Peninsula, *Geosci. J.* **10**, no. 4, 491–497.
- Kaneko, Y., and P. M. Shearer (2015). Variability of seismic source spectra, estimated stress drop, and radiated energy, derived from cohesive-zone models of symmetrical and asymmetrical circular and elliptical ruptures, *J. Geophys. Res.* **120**, no. 2, 1053–1079.
- Kee, W.-S., S. Kim, H. Kim, P. Hong, C. Kwon, H.-J. Lee, D.-L. Cho, H. Hoh, K.-Y. Song, and U. Byun (2019). Geologic Map of Korea (1:1,000,000), Korea Institute of Geoscience and Mineral Resources, doi: [10.22747/data.20220816.4826](https://doi.org/10.22747/data.20220816.4826).
- Kim, S. J., and S. G. Kim (1983). A study on the crustal structure of South Korea by using seismic waves, *Econ. Environ. Geol.* **16**, no. 1, 51–61.
- Kim, W.-Y., H. Choi, and M. Noh (2010). The 20 January 2007 Odaesan, Korea, earthquake sequence: Reactivation of a buried strike-slip fault? *Bull. Seismol. Soc. Am.* **100**, no. 3, 1120–1137.
- Kim, W.-Y., M.-S. Seo, J. Y. Park, S. Han, Y. O. Son, and Y. Kim (2023). The 28 October 2022  $M_w$  3.8 Goesan earthquake sequence in Central Korea: Stress drop, aftershock triggering, and fault interaction, *Bull. Seismol. Soc. Am.* **113**, no. 6, 2416–2431.
- Klein, F. W. (2002). User's guide to HYPOINVERSE-2000, a Fortran program to solve for earthquake locations and magnitudes, *Open-File Rept.* 02-171.
- Lanza, V., D. Spallarossa, M. Cattaneo, D. Bindi, and P. Augliera (1999). Source parameters of small events using constrained deconvolution with empirical Green's functions, *Geophys. J. Int.* **137**, no. 3, 651–662.
- Lee, S., A. Saxena, J. H. Song, J. Rhie, and E. Choi (2022). Contributions from lithospheric and upper-mantle heterogeneities to upper crustal seismicity in the Korean Peninsula, *Geophys. J. Int.* **229**, no. 2, 1175–1192.
- Li, J., T. Kim, N. Lapusta, E. Biondi, and Z. Zhan (2023). The break of earthquake asperities imaged by distributed acoustic sensing, *Nature* **620**, no. 7975, 800–806.
- Madariaga, R. (1976). Dynamics of an expanding circular fault, *Bull. Seismol. Soc. Am.* **66**, no. 3, 639–666.
- Marsan, D., and O. Lengline (2008). Extending earthquakes' reach through cascading, *Science* **319**, no. 5866, 1076–1079.
- McGuire, J. J. (2004). Estimating finite source properties of small earthquake ruptures, *Bull. Seismol. Soc. Am.* **94**, no. 2, 377–393.
- McGuire, J. J. (2017). A MATLAB toolbox for estimating the second moments of earthquake ruptures, *Seismol. Res. Lett.* **88**, no. 2A, 371–378.
- Mendoza, C., and S. Hartzell (2013). Finite-fault source inversion using teleseismic P waves: Simple parameterization and rapid analysis, *Bull. Seismol. Soc. Am.* **103**, no. 2A, 834–844.

- Meng, H., J. J. McGuire, and Y. Ben-Zion (2020). Semiautomated estimates of directivity and related source properties of small to moderate Southern California earthquakes using second seismic moments, *J. Geophys. Res.* **125**, no. 4, doi: [10.1029/2019JB018566](https://doi.org/10.1029/2019JB018566).
- Meng, Q., S. Ni, and Z. Peng (2021). Complex source behaviors and spatiotemporal evolution of seismicity during the 2015–2016 earthquake sequence in Cushing, Oklahoma, *J. Geophys. Res.* **126**, no. 6, doi: [10.1029/2021JB022168](https://doi.org/10.1029/2021JB022168).
- Mori, J., and A. Frankel (1990). Source parameters for small events associated with the 1986 North Palm Springs, California, earthquake determined using empirical Green functions, *Bull. Seismol. Soc. Am.* **80**, no. 2, 278–295.
- Neves, M., L. Y. Chuang, W. Li, Z. Peng, P. M. Figueiredo, and S. Ni (2024). Complex rupture dynamics of the extremely shallow August 2020 M5.1 Sparta, North Carolina earthquake, *Commun. Earth Environ.* **5**, no. 1, doi: [10.1038/s43247-024-01316-8](https://doi.org/10.1038/s43247-024-01316-8).
- Pennington, C. N., H. Chang, J. L. Rubinstein, R. E. Abercrombie, N. Nakata, T. Uchide, and E. S. Cochran (2022). Quantifying the sensitivity of microearthquake slip inversions to station distribution using a dense nodal array, *Bull. Seismol. Soc. Am.* **112**, no. 3, 1252–1270.
- Pennington, C. N., T. Uchide, and X. Chen (2022). Slip characteristics of induced earthquakes: Insights from the 2015  $M_w$  4.0 Guthrie, Oklahoma earthquake, *J. Geophys. Res.* **127**, no. 5, doi: [10.1029/2021JB023564](https://doi.org/10.1029/2021JB023564).
- Ross, Z. E., H. Kanamori, and E. Hauksson (2017). Anomalously large complete stress drop during the 2016  $M_w$  5.2 Borrego Springs earthquake inferred by waveform modeling and near-source aftershock deficit, *Geophys. Res. Lett.* **44**, no. 12, 5994–6001.
- Saikia, C. K. (1994). Modified frequency-wavenumber algorithm for regional seismograms using Filon's quadrature: Modelling of  $Lg$  waves in eastern North America, *Geophys. J. Int.* **118**, no. 1, 142–158.
- Saikia, C. K., and D. V. Helmberger (1997). Approximation of rupture directivity in regional phases using upgoing and downgoing wave fields, *Bull. Seismol. Soc. Am.* **87**, no. 4, 987–998.
- Sambridge, M. (1999). Geophysical inversion with a neighbourhood algorithm—I. Searching a parameter space, *Geophys. J. Int.* **138**, no. 2, 479–494.
- Silver, P. (1983). Retrieval of source-extent parameters and the interpretation of corner frequency, *Bull. Seismol. Soc. Am.* **73**, no. 6A, 1499–1511.
- Snook, J. A. (2003). FOCMEC: FOCal MEChanism determinations, in *International Handbook of Earthquake and Engineering Seismology, Part B*, W. H. K. Lee, H. Kanamori, P. C. Jennings, and C. Kisslinger (Editors), Academic Press, London, United Kingdom, 1629–1630.
- Soh, I., C. Chang, J. Lee, T.-K. Hong, and E. S. Park (2018). Tectonic stress orientations and magnitudes, and friction of faults, deduced from earthquake focal mechanism inversions over the Korean Peninsula, *Geophys. J. Int.* **213**, no. 2, 1360–1373.
- Somerville, P., K. Irikura, R. Graves, S. Sawada, D. Wald, N. Abrahamson, Y. Iwasaki, T. Kagawa, N. Smith, and A. Kowada (1999). Characterizing crustal earthquake slip models for the prediction of strong ground motion, *Seismol. Res. Lett.* **70**, no. 1, 59–80.
- Song, S. G., and B. Duan (2024). Dynamic rupture models of the 2016  $M_L$  5.8 Gyeongju, South Korea, earthquake, constrained by a kinematic rupture model and seismic waveform data, *Bull. Seismol. Soc. Am.* **114**, no. 2, 710–725.
- Song, X. J., and D. V. Helmberger (1996). Source estimation of finite faults from broadband regional networks, *Bull. Seismol. Soc. Am.* **86**, no. 3, 797–804.
- Taira, T. A., D. S. Dreger, and R. M. Nadeau (2015). Rupture process for micro-earthquakes inferred from borehole seismic recordings, *Int. J. Earth Sci.* **104**, 1499–1510, doi: [10.1007/s00531-015-1217-8](https://doi.org/10.1007/s00531-015-1217-8).
- Toda, S., R. S. Stein, V. Sevilgen, and J. Lin (2011). Coulomb 3.3 Graphic-rich deformation and stress-change software for earthquake, tectonic, and volcano research and teaching—User guide, *U.S. Geol. Surv. Open-File Rept. 2011-1060*, 63 pp.
- Twardzik, C., R. Madariaga, S. Das, and S. Custódio (2012). Robust features of the source process for the 2004 Parkfield, California, earthquake from strong-motion seismograms, *Geophys. J. Int.* **191**, no. 3, 1245–1254.
- Uchide, T., and S. G. Song (2018). Fault rupture model of the 2016 Gyeongju, South Korea, earthquake and its implication for the underground fault system, *Geophys. Res. Lett.* **45**, no. 5, 2257–2264.
- Uieda, L., D. Tian, W. J. Leong, L. Toney, W. Schlitzer, M. Grund, D. Newton, M. Ziebarth, M. Jones, and P. Wessel (2021). PyGMT: A Python interface for the Generic Mapping Tools (v0.9.0), *Zenodo*, doi: [10.5281/zenodo.8303186](https://doi.org/10.5281/zenodo.8303186).
- Vallée, M., and M. Bouchon (2004). Imaging coseismic rupture in far field by slip patches, *Geophys. J. Int.* **156**, no. 3, 615–630.
- Vera, F., F. Tilmann, and J. Saul (2024). A decade of short-period earthquake rupture histories from multi-array back-projection, *J. Geophys. Res.* **129**, no. 2, doi: [10.1029/2023JB027260](https://doi.org/10.1029/2023JB027260).
- Viegas, G., R. E. Abercrombie, and W.-Y. Kim (2010). The 2002 M5 Au Sable Forks, NY, earthquake sequence: Source scaling relationships and energy budget, *J. Geophys. Res.* **115**, no. B7, doi: [10.1029/2009JB006799](https://doi.org/10.1029/2009JB006799).
- Waldhauser, F., and W. L. Ellsworth (2000). A double-difference earthquake location algorithm: Method and application to the northern Hayward fault, California, *Bull. Seismol. Soc. Am.* **90**, no. 6, 1353–1368.
- Wessel, P., J. F. Luis, L. Uieda, R. Scharroo, F. Wobbe, W. H. F. Smith, and D. Tian (2019). The generic mapping tools version 6. *Geochem. Geophys. Geosys.* **20**, no. 11, 5556–5564.
- Wössner, J., D. Schorlemmer, S. Wiemer, and P. M. Mai (2006). Spatial correlation of aftershock locations and on-fault main shock properties, *J. Geophys. Res.* **111**, no. B8, doi: [10.1029/2005JB003961](https://doi.org/10.1029/2005JB003961).
- Wu, Q., and M. Chapman (2017). Stress-drop estimates and source scaling of the 2011 Mineral, Virginia, mainshock and aftershocks, *Bull. Seismol. Soc. Am.* **107**, no. 6, 2703–2720.
- Yao, S., Z. Yang, and H. Yang (2025). Determination of rupture directivity of the 2024 Feidong M4.7 earthquake using Single Near-Source Station, *Earthq. Sci.* **38**, no. 5, 399–407.
- Žilić, I., M. Causse, M. Vallée, and S. Markušić (2025). High stress drop and slow rupture during the 2020  $M_w$  6.4 intraplate Petrinja Earthquake, Croatia, *J. Geophys. Res.: Solid Earth* **130**, no. 1, doi: [10.1029/2024JB029107](https://doi.org/10.1029/2024JB029107).

Manuscript received 7 August 2025  
Published online 11 December 2025